Article:

eprints@whiterose.ac.uk
https://eprints.whiterose.ac.uk/

ORIGINAL ARTICLE

An empirical method for modelling the secondary shock from high explosives in the far-field

S. E. Rigby[1,2] · E. Mendham[1] · D. G. Farrimond[1,3] · E. G. Pickering[4] · A. Tyas[1,3] · G. Pezzola[5]

Abstract

As the detonation product cloud from a high explosive detonation expands, an arresting flow is generated at the interface between these products and the surrounding air. Eventually this flow forms an inward-travelling shock wave which coalesces at the origin and reflects outwards as a secondary shock. Whilst this feature is well known and often reported, there remains no established method for predicting the form and magnitude of the secondary shock. This paper details an empirical superposition method for modelling the secondary shock, based on the physical analogy of the secondary loading pulse resembling the blast load from a smaller explosive relative to the original. This so-called dummy charge mass is determined from 58 experimental tests using PE4, PE8, and PE10, utilising Monte Carlo sampling to account for experimental uncertainty, and is found to range between 3.2–4.9% of the original charge mass. A further 18 "unseen" datapoints are used to rigorously assess the performance of the new model, and it is found that reductions in mean absolute error of up to 40%, and typically 20%, are achieved compared to the standard model which neglects the secondary shock. Accuracy of the model is demonstrated across a comprehensive range of far-field scaled distances, giving a high degree of confidence in the new empirical method for modelling the secondary shock from high explosives.

Keywords Blast loading · Empirical method · Monte Carlo sampling · Secondary shock · Superposition

1 Introduction

1.1 Theoretical background

The secondary shock is a well-known feature in blast pressure histories from high explosive detonations and has been observed in pressure traces [1–4], high-speed flow visualisation [5, 6], analytical [7–9], and numerical work [10]. Even

✉ S. E. Rigby
  sam.rigby@sheffield.ac.uk

1 Department of Civil & Structural Engineering, University of Sheffield, Mappin Street, Sheffield S1 3JD, UK

2 Arup Resilience, Security & Risk, 3 Piccadilly Pl, Manchester M1 3BN, UK

3 Blastech Ltd., The Innovation Centre, 217 Portobello, Sheffield S1 4DP, UK

4 Cranfield Forensic Institute, Cranfield University, Defence Academy of the United Kingdom, Shrivenham SN6 8LA, UK

5 US Army Engineer Research and Development Centre (ERDC), Halls Ferry Rd, Vicksburg, MS, USA

tertiary shocks[1] have been identified in some pressure traces with low signal noise [11].

The secondary shock is distinct from, and should not be confused with, other instances of secondary loading pulses in pressure traces, including those from: bridging waves from non-spherical charges [12]; reflection of the primary shock off the contact interface between the air and detonation product cloud in close-in-blast scenarios [13, 14]; and successive reflections in confined environments [15, 16].

The term "secondary shock" is often used to describe these features. However, the focus of this manuscript is on a particular type of secondary shock, formed according to the process outlined below and shown indicatively in Fig. 1.

(a) **Generation:** As the contact surface between the detonation product cloud (DPC) and surrounding air begins to decelerate due to over-expansion [3], the secondary shock is formed, initially as an "arrester" flow [17], sharply reducing the pressure at the edge of the DPC.

---

[1] As lightheartedly noted in Ref. [11], the secondary and tertiary shocks were sometimes referred to as "pete" and "repete".
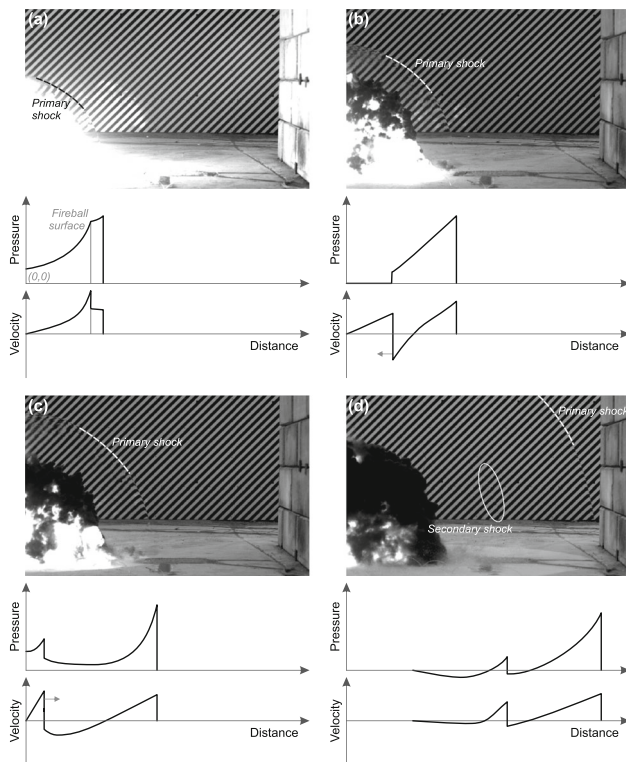
Fig. 1 The four stages of secondary shock formation: **a** generation; **b** inward collapse; **c** re-expansion; and **d** propagation. Each stage is represented by a high-speed video frame ([19]) together with a pressure and velocity plot (derived from Ref. [17]). Note that a negative velocity value indicates inward flow at that location, with the secondary shock propagation direction indicated. The primary shock location has been annotated in each frame along with the secondary shock where visible

(b) **Inward collapse:** As the DPC continues to over-expand, the "backward-facing" velocity of the secondary shock begins to exceed the outflow velocity of the DPC, and the pressure wave travels backwards towards the origin.

(c) **Re-expansion:** The pressure wave eventually coalesces, or implodes, at the origin and is reflected outwards.

(d) **Propagation:** The secondary shock continues to expand outwards, eventually emerging out of the DPC[2] and propagating in free air behind the primary shock. The secondary shock is clearly visible as a distinct shock front in pressure traces and high-speed video.

Originating from within, and initially propagating through, the DPC, or "fireball", the secondary shock encodes important information about the state of the early-time detonation products and, ultimately, the explosive itself. In the same way that cosmic microwave background (CMB) radiation—"*the*

cooled remnant of the first light that could ever travel freely throughout the Universe*" [20]—allows scientists to understand the early properties of the Universe some 13.7 billion years after the Big Bang, the same can be said about the secondary shock and its importance in understanding properties of the explosion from which it originated. If CMB radiation is an "*echo of the Big Bang*", the secondary shock is an echo of a much smaller bang.

1.2 Literature review

Gitterman [21] compiled secondary shock delay times, defined as the difference between arrival of primary and secondary shocks, from numerous sources, with charge masses ranging from 360 kg to 2.47 kt. This work was extended by Rigby and Gitterman [22], who introduced smaller scale data (0.25 kg) and derived a scaling law based on explosive properties such as mass, packing density, and velocity of detonation. This effectively normalised delay times by a "*characteristic time of complete detonation of a finite hemispherical charge*", specifically the time taken for a detonation wave to traverse the radius of the charge.[3] The relations provided a predictive method whereby one of yield, density, and velocity of detonation could be determined with knowledge of the secondary shock delay and the other two parameters. This predictive model has since been used to estimate the yield of a firework factory explosion [23].

Because of the dependency of the secondary shock arrival time on the energetic state (and sonic velocity) of the cooling detonation product fireball, it has been suggested that the secondary shock delay time can be used to determine whether complete or incomplete detonation has occurred [1]. Furthermore, the secondary shock delay has been used to study the effects of secondary combustion (often termed "afterburn") of the reaction products, an aspect of modelling which is "*typically very poorly dealt with*", and "*is significantly affected by the local heating and conditions present in the ongoing late-time reactions through which the inward release and outgoing shock pass*" [24].

Schwer and Rigby [25, 26] performed numerical analysis to calibrate the energy release rate of secondary reactions using published experimental data [27, 28]. Notably, when reaction rates were calibrated to bring the modelled secondary shock in-line with experimental data for simple incident or normally reflected groundbursts, the secondary shock arrival time was overpredicted for height-of-burst scenarios. This suggests that reflection of the primary shock off

---

[2] Whilst the DPC may have partially equilibrated with the surrounding air, any slight impedance mismatch will cause a proportion of the secondary shock to be reflected back towards the origin, to again coalesce and reflect outwards as a tertiary shock [18].

[3] It was justified that the delay between the expansion wave forming at the periphery of the charge and imploding at the centre would be strongly correlated to this time, since the velocity of this wave would be correlated to the detonation velocity, thereby providing a physical validity to this scaling.

the nominally rigid ground surface enhances afterburn and therefore locally increases the pressure and energy, and hence soundspeed, in the detonation product cloud, supporting the findings in Tyas et al. [29].

Despite the arrival time of the secondary shock being seemingly well predicted, there remains no method for accurately quantifying an accurate temporal history of a blast load which includes the contribution of the secondary shock. Whilst methods such as Gaussian process modelling [30] can incorporate discontinuities such as the secondary shock, they still require the arrival time of this discontinuity to be known a priori and therefore cannot be considered a true predictive approach.

A possible reason for the lack of research into the secondary shock is that experimental measurements of the negative phase are subjected to issues which are either not present or not significant in the positive phase, such as low signal-to-noise ratios, longer-term sensor drift, and the arrival of reflected waves from nearby surroundings. As noted by Bogosian et al. [31] in their review of uncertainty and conservatism in simplified blast models, "*(t)he precise provenance of these* [negative phase] *curves is unknown at the present time*", with the suggestion that this is due in-part to the fact that "*(n)ot all* [experimental data records] *were of sufficient duration and/or quality as to be able to extract negative as well as positive values, and while some had dubious peak pressure readings, others became suspect at later time and therefore could not produce reliable impulses*". The technical manual UFC 3-340-02 [32], *Structures to resist the effects of accidental explosions*, mentions the term "secondary shock" only once, and that is in reference to additional reflected shocks when quantifying confined, rather than free-field, blast loading.

As noted by Sadwin and Swisdak Jr. [4], "*the secondary shock which occurs near the minimum of the negative phase… deserves further attention*". This limitation is also noted by Ehrhardt et al. [33], in the context of predictive approaches for air blast above the triple point: "*Investigation of this phenomenon* [the secondary shock] *would help to increase the accuracy of the existing empirical models*".

Sadwin and Swisdak Jr. [4] go on to state that "*for structural elements exposed at low pressures, the secondary shock could be very important*". This was particularly the case in the study by Hatfield et al. [34], where accurate quantification of the entire form and magnitude of the negative phase, inclusive of the secondary shock, was described as being "*critical for accurate fragment velocity calculation*" when measuring the response of unreinforced concrete masonry walls subjected to blast loading.

1.3 Overview of approach

The aim of this paper is therefore to develop a new empirical method for modelling the secondary shock in the far-field. A total of 76 experimental measurements of the secondary shock from medium-scale[4] laboratory testing of plasticised high explosives are used to develop a novel predictive methodology. According to this approach, the secondary shock is modelled as the additional loading from a smaller "dummy" charge at some fraction of the original charge mass, with the principle of superposition used to create the combined loading history. This approach is similar to superposition methods used in simplified load predictors for blast in complex environments [35, 36], but distinct in the sense that it is based on a surrogate form of the underlying physics of the problem, i.e., treating the secondary shock as a genuine explosion, only from some lesser charge mass.

The remainder of the paper is structured as follows. First, an overview of the conceptual model is presented, including a description of the standard methods for predicting and modelling the positive and negative phase, as well as a detailed formulation of the new superposition model. Next, the available experimental data are introduced, and extracted secondary shock parameters are evaluated and discussed. Monte Carlo sampling is then used to determine the empirical parameters for use in the new model, and finally performance of the new model is rigorously assessed against unseen test data.

2 Conceptual model and experimental dataset

2.1 UFC positive and negative phase

An idealised blast pressure history, shown in Fig. 2a, is characterised by a near-discontinuous increase in pressure above atmospheric pressure (termed "overpressure"), followed by an exponential decay back to ambient conditions. Immediately after the period of positive overpressure (the "positive phase") is a negative overpressure phase (the "negative phase"); a partial vacuum caused by over-expansion of the shocked air [37]. Subsequently, the pressure returns to ambient and the loading event is considered complete.

Key loading parameters indicated in Fig. 2a are:

- Peak positive phase pressure, p^+
- Peak negative phase pressure, p^-
- Arrival time, t_a
- Positive phase duration, t_d^+
- Negative phase duration, t_d^-

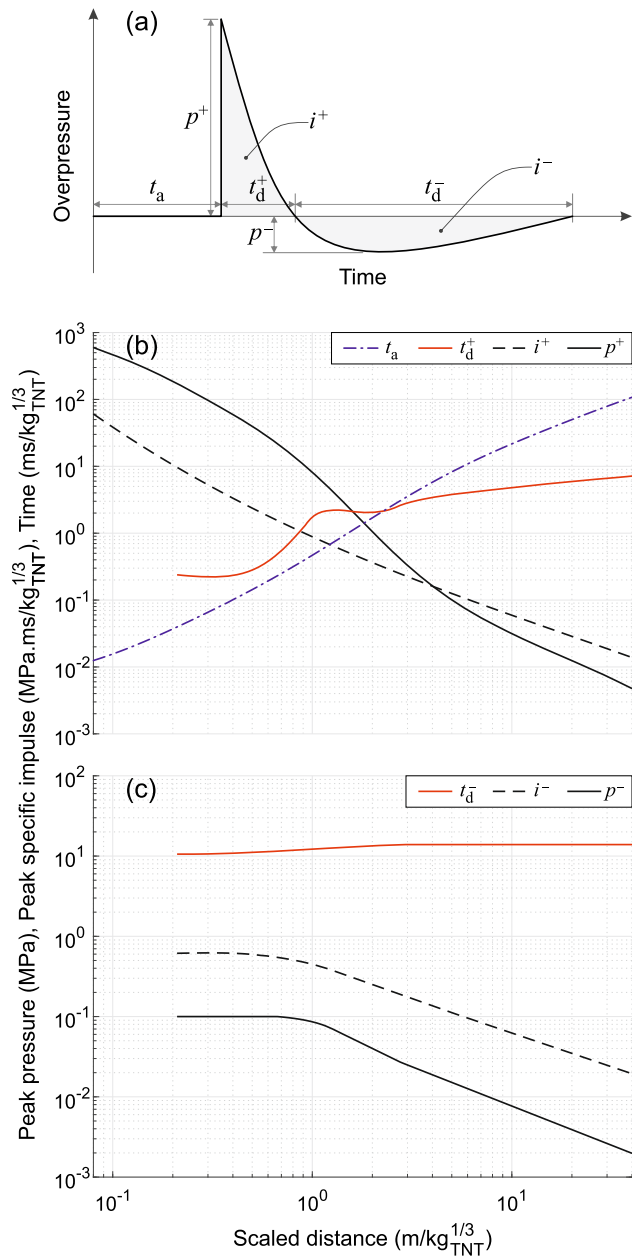[4] 180–350 g explosives at 2–10 m, see Table 2.

Fig. 2 Graphs showing the idealised blast loading as in UFC 3-340-02 for hemispherical charges: **a** idealised pressure–time history with the key parameters annotated; **b** positive phase parameters relations; and **c** negative phase parameters relations

– Positive phase specific impulse, i^+ (integral of positive phase pressure with respect to time)
– Negative phase specific impulse, i^- (integral of negative phase pressure with respect to time)

These loading parameters are readily predicted using relationships presented in UFC 3-340-02 [32], repeated in Fig. 2b and c for positive and negative phase parameters, respectively. These relationships make use of Hopkinson-

Cranz [38, 39], or "cube-root", scaling via the parameter known as scaled distance:

$$Z = R/W^{1/3} \tag{1}$$

where Z is scaled distance, R is the distance from the blast source to the point of interest (m), and W is the mass of explosives (kg), expressed as an equivalent mass of TNT using the concept of TNT equivalence [40], labelled TNT_e.[5] As such, the terms in (1) are often given the subscript TNT. Note that whilst the terminology in Fig. 2a makes no distinction between incident and reflected parameters, those displayed in Fig. 2b and c are reflected parameters and these are the focus of the remainder of this paper.

The choice of the UFC relationships (and associated scaling law) as a baseline model is supported by numerous controlled experimental studies which confirm it to have high accuracy [41–45], self-similarity [46], physical basis [47], and low model error in the far-field [48]. For an extended discussion on this topic, the reader is directed to Ref. [49].

The positive phase pressure history is typically described by the "modified Friedlander" equation [50], and the negative phase by the Granström cubic relationship[6] [52]:

$$p(t) = \begin{cases} 0, & \hat{t} < 0 \\ p^+ \left(1 - \hat{t}/t_d^+\right) \exp\left(-\alpha \hat{t}/t_d^+\right) & 0 \leq \hat{t} < t_d^+ \\ -p^- \left(27\check{t}/4t_d^-\right) \left(1 - \check{t}/t_d^-\right)^2 & 0 \leq \check{t} < t_d^- \\ 0, & \check{t} \geq t_d^- \end{cases} \tag{2}$$

where $\hat{t} = t - t_a$, and $\check{t} = t - (t_a + t_d^+)$.

Defining $\hat{t}$ and $\check{t}$ as time during the positive and negative phases, respectively, allows the relations in (2) to be presented in a more compact manner.

The positive phase specific impulse, i^+, negative phase specific impulse, i^-, and net specific impulse, $i_{net} = i^+ + i^-$, can therefore be calculated:

$$i^+ = \int_0^{t_d^+} p(t) d\hat{t} = \frac{p^+ t_d^+}{\alpha^2} (\alpha - 1 + \exp[-\alpha]) \tag{3}$$

$$i^- = \int_0^{t_d^-} p(t) d\check{t} = -\frac{9 p^- t_d^-}{16} \tag{4}$$

$$i_{net} = \frac{p^+ t_d^+}{\alpha^2} (\alpha - 1 + \exp[-\alpha]) - \frac{9p^- t_d^-}{16} \quad (5)$$

The term α in (2) and (3) is known as the waveform parameter, or decay coefficient [53], and controls the decay rate of the positive phase. This allows for an exact value of impulse to be achieved for a given peak pressure and positive phase duration; however, in practise all three are known and α is determined by rearranging (3) and solving iteratively:

$$\alpha = \frac{p^+ t_d^+}{\alpha i^+} (\alpha - 1 + \exp[-\alpha]) \quad (6)$$

Similarly, the negative phase peak pressure and impulse are typically known (or predicted), and it is the negative phase duration which is determined by rearranging the integral of the negative phase history, i.e.,

$$t_d^- = \frac{16 i^-}{9 p^-}. \quad (7)$$

2.2 Proposed model

A new set of parameters are introduced, relating specifically to the secondary shock, as indicated in Fig. 3a. Namely:

– Peak secondary shock pressure, p^*
– Secondary shock arrival time, t_a^*
– Secondary shock duration, t_d^*
– Secondary shock specific impulse, i^*

Based on the rationalisation that the secondary shock is analogous to a secondary explosion from a source term with the same (spatial) origin but lower mass than the original explosion, the proposed combined pressure history, accounting for the secondary shock, is outlined conceptually in Fig. 3b–d. In short, Fig. 3b represents the standard model, whose form is a function of charge mass and stand-off distance as described above: $f(R, W_{TNT})$.

Figure 3c shows an additional loading feature to model the secondary shock: $g(R, cW_{TNT}, dt_{lag})$, where c and dt_{lag} are empirically determined parameters for scaling down the original charge mass and correcting for model error in arrival time predictions,[7] respectively. Finally, Fig. 3d represents the proposed model given as summation of the two loading histories: $f + g$.

---

[7] Previous related studies have indicated that it is not possible to exactly match peak pressure *and* arrival times when modelling secondary loading features with dummy or mirror charges [54].
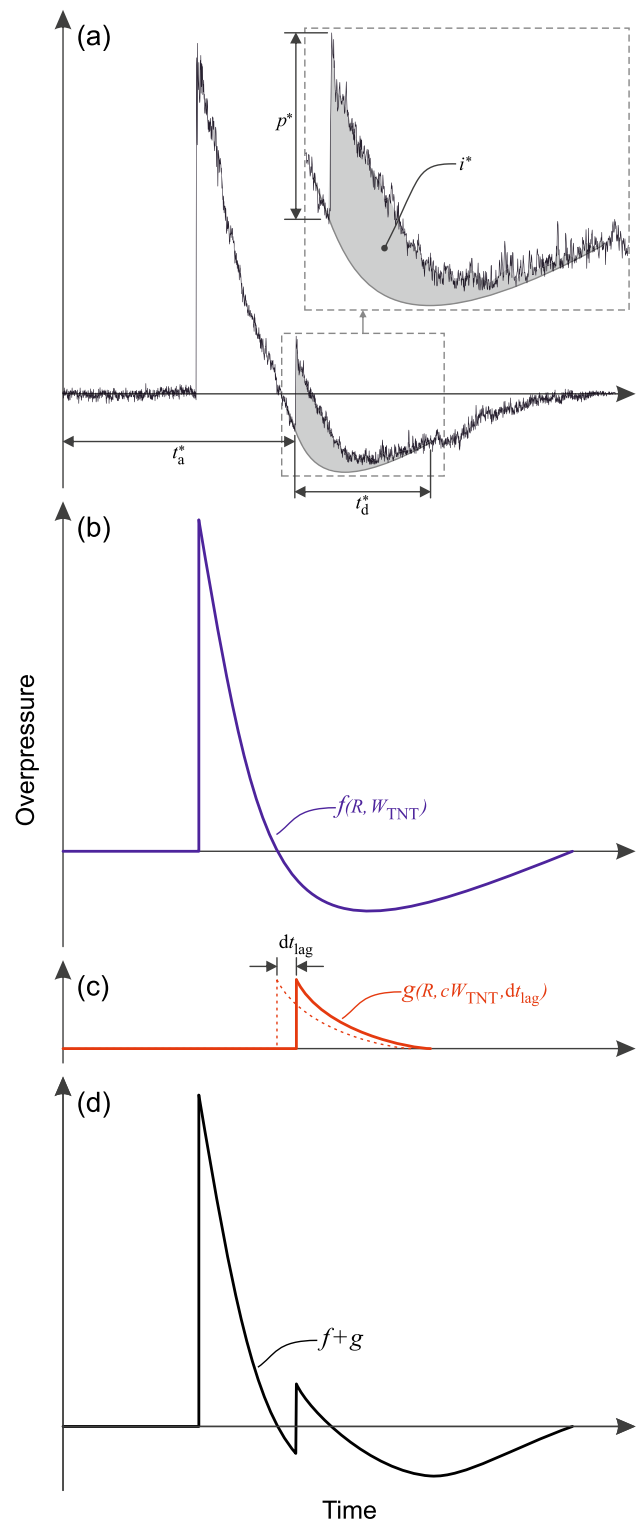
Fig. 3 Graphs showing the proposed secondary shock model: **a** experimental pressure trace with the secondary shock parameters labelled; **b** standard idealised positive and negative phase histories for a charge of known weight, W_{TNT} and stand-off distance, R; **c** secondary shock loading modelled as a scaled dummy charge, cW with an offset arrival time, dt_{lag}, and; **d** superposition of the primary and secondary shock pressure histories

The time history of the secondary shock pressure, p_{SS}, is therefore defined as:

$$p_{SS}(t) = \begin{cases} 0, & \tau < 0 \\ p^* \left(1 - \tau/t_d^*\right) \exp\left(-\beta\tau/t_d^*\right) & 0 \leq \tau < t_d^* \\ 0, & \tau \geq t_d^* \end{cases} \quad (8)$$

where $\tau = t - (t_a^* + dt_{lag})$.

Note, parameters here are given the superscript $*$ to distinguish from those associated with the primary shock, with the exception of β, which serves the same purpose as α but whose value will differ for a given $[R, W]$ pair.

Finally, the net specific impulse of the new model is given as:

$$\begin{aligned} i_{net}^* &= i_{net} + \int_0^{t_d^*} p_{SS}(t) d\tau \\ &= \frac{p^+ t_d^+}{\alpha^2} (\alpha - 1 + \exp[-\alpha]) - \frac{9p^-}{16t_d^-} \\ &\quad + \frac{p^* t_d^*}{\beta^2} (\beta - 1 + \exp[-\beta]) \end{aligned} \quad (9)$$

2.3 Assumptions

The following assumptions have been made to facilitate development of the new model:

– The explosive is formed into a hemisphere, detonated on a flat, rigid reflecting surface, such that no additional reflected waves exist (i.e., those reflected off the ground in a height-of-burst scenario, or internal bridging waves from shape effects caused by non-(hemi)spherical charges [55]).
– A single value of TNT equivalence is deemed appropriate for far-field blast parameter prediction, as discussed in Ref. [56].
– The explosive is considered "ideal", i.e., the energetic release can be considered near-instantaneous and it is relatively oxygen-balanced such that no significant secondary combustion (or "afterburning") occurs during the formation and re-expansion of the secondary shock.[8]
– The reflected wave from the primary shock is sufficiently weak in magnitude to not substantially alter the form and magnitude of the secondary shock once the two waves interact some distance prior to the secondary shock impinging on the loaded surface.

---

[8] Afterburn has a negligible effect on the hydrostatic pressure and density of the primary shock, but it can significantly influence the particle velocity in the later stages of the positive phase. As a result, reversal of the particle flow occurs later than in ideal explosives, propagation of the secondary shock is enhanced, and it is able to progress into the positive phase [57].

Table 1 Properties of PE4, PE8, and PE10 explosives [61]

	PE4	PE8	PE10
Explosive	RDX	RDX	PETN
Relative mass	88%	86.5%	86%
Density (kg/m^3)	1590	1570	1550
Specific energy (MJ/kg)	5120	5080	4980
Detonation velocity (m/s)	8035	7948	7735
TNT$_e$	1.22	1.24	1.22

– Model parameters c and dt_{lag} are derived for far-field loading only, i.e., $Z > 2.0$ m/kg$^{1/3}$ [58], are assumed to be constant in this range, and independent of physical scale.[9]

2.4 Experimental dataset

The empirical parameters c and dt_{lag} are determined and validated using pre-existing experimental datasets [37, 45, 60]. These experiments were performed at the University of Sheffield Blast and Impact Laboratory using hemispheres of plastic explosives: PE4, PE8, and PE10. PE4 and PE8 are RDX-based, whereas PE10 is PETN-based. All explosive types are formed of between 86–87% explosive by mass, with the remainder being mineral oil binder [58]. Anecdotally, the different binders used in PE4 and PE8 result in different levels of texture and malleability: PE8 is slightly sticky but much more workable, whereas PE4 is slightly crumbly and less workable. Relevant explosive characteristics are summarised in Table 1.

The explosive charges were formed using bespoke 3D-printed charge moulds. All charges were detonated at the bottom-centre. In [37, 60], this was achieved by inserting the detonator through the depth of the charge from above ("top-detonated"), whereas in more recent work [45] the detonator was inserted slightly into the charge from beneath ("bottom-detonated"). The top- and bottom-detonated charges were each sat on a small steel plate. In the top-detonated cases, this plate was sat directly on a flat-reinforced concrete ground slab. In the bottom-detonated cases, the plates (with a pre-formed hole in the centre) were sat flush to the surface of a small sand-filled channel, which was cut through the centre of the ground slab.

In both cases, a break-wire was wrapped around the detonator to trigger the data capture and enable the arrival time to be determined relative to the gauge signals. The detonator cables and break-wire were run through the channel ensuring that there were no obstructions between the charge and

---

[9] Recent work has confirmed this to be the case [59].

the measurement location. The ground slab was swept clean after each test.

Pressure was measured using surface-mounted Kulite HKM(M) 7-bar piezoresistive pressure gauges, which were threaded through small steel plates affixed at ground level to the outer surface of a nominally rigid reflecting wall. The miniaturised sensors have an 8.1-mm presented area and a high natural frequency (> 400 kHz) making them suitable for recording shock pressures. Data were recorded at between 100–200 kHz with a 16-bit resolution.

In [37, 60], the charge was placed at set distances from a blockwork-covered reinforced concrete bunker wall. In [45], an additional blockwork wall was introduced 10.0 m from, and parallel to, the existing bunker wall, meaning that pressure could be recorded at pairs of stand-off distances, typically at 1-m increments (i.e., 2 m and 8 m, 3 m and 7 m, etc.). Both walls were $\sim$ 4-m high, ensuring that any clearing rarefaction waves would arrive towards the end of the negative phase or after, and their contribution to the blast pressure history would be negligible [62].

Data from Ref. [45] are used to generate the empirical values of c and dt_{lag} (58 datapoints in total, termed the "train" dataset), whereas data from [37, 60] are used to subsequently assess the performance of the new method against unseen data (the remaining 18 datapoints, termed the "test" dataset); an approximate 75:25 split. A summary of the experiments is provided in Table 2.

2.5 Experimentally measured values

Secondary shock parameters were determined manually using a point-picking method. Whilst automated techniques for determining positive phase blast load parameters have been used previously with some success [63, 64], these require fitting a function (typically a modified Friedlander) to the latter part of the pressure history and back-extrapolating to arrival time. Since the secondary shock acts during the negative phase, the superposition of two complex and unknown functions limits the applicability of such methods.

Further, automatically defining the end time of the secondary shock (and therefore duration, t_d^*) is non-trivial since this pressure value does not coincide with the origin, as it does to mark the end of the positive phase. Some element of human judgement is necessary to deem when pressures have returned to the original form of the negative phase following the secondary shock, and this varies from test to test.

Secondary shock specific impulse was calculated as the area of the triangle with length t_d^* and height p^* and is therefore subject to the same degree of subjectivity. However, when calculating experimental net impulse, no such approximation is required and instead the pressure trace can simply be integrated in its current form.

Secondary shock parameters for the training dataset [45] are shown in Fig. 4. Peak pressure and peak specific impulse appear to follow an exponential decrease with increasing scaled distance, similar to the original Kingery and Bulmash [65] and UFC [32] relations, giving confidence that the dummy charge approach is appropriate.

Arrival times appear to follow a linear trend, which is expected given that the secondary shock is likely to be travelling at sonic velocity in the far-field. Secondary shock duration appears relatively constant, albeit with considerable spread, which in-turn results in similar levels of variability in the measured specific impulse values. Both of these are due to subjectivity in determining the true end of the secondary shock loading pulse. When considering the net impulse of the experimental trace, it is expected that this spread will reduce as the subjectivity associated with defining duration will be avoided.

Since peak pressure and arrival time are clearly the more consistent measures, it is appropriate that these are the two parameters from which c and dt_{lag} are to be determined. However, it is acknowledged that these parameters are less consistent and exhibit a greater spread than is typically seen for positive phase parameters (see [37]), in-part due to lower signal-to-noise.

3 Empirical model parameters: c and dt_{lag}

3.1 Monte Carlo sampling

In order to account for uncertainty in each experimental parameter—epistemic uncertainty in input variables R and W, and aleatoric uncertainty in output variables p^* and t_d^*—Monte Carlo sampling was used. Briefly, this requires each parameter to be formed into a representative statistical distribution, with the empirical parameters derived from fits to the (much larger quantity of) *sampled* data.

Charge mass was deemed to be accurate to within ± 0.1 g, and stand-off distance to within ± 3 mm. Hence, samples were drawn from uniform distributions within these bounds, centred on the experimental input value (which is termed y hereafter).

For each experimental trace, the standard deviation of the pre-arrival signal was calculated. This was found to range typically between 0.4–0.6 kPa, with a small number of values approaching 0.7 kPa.[10] Hence, each experimentally measured peak pressure was sampled from a normal distribution with a mean of y and a standard deviation of 0.7.

Finally, when determining arrival time, these were taken as the sample point at the *beginning* of the rise to peak sec-

---

[10] Due to slight differences in the setup of each test including weather conditions, signal noise, cable length, etc.
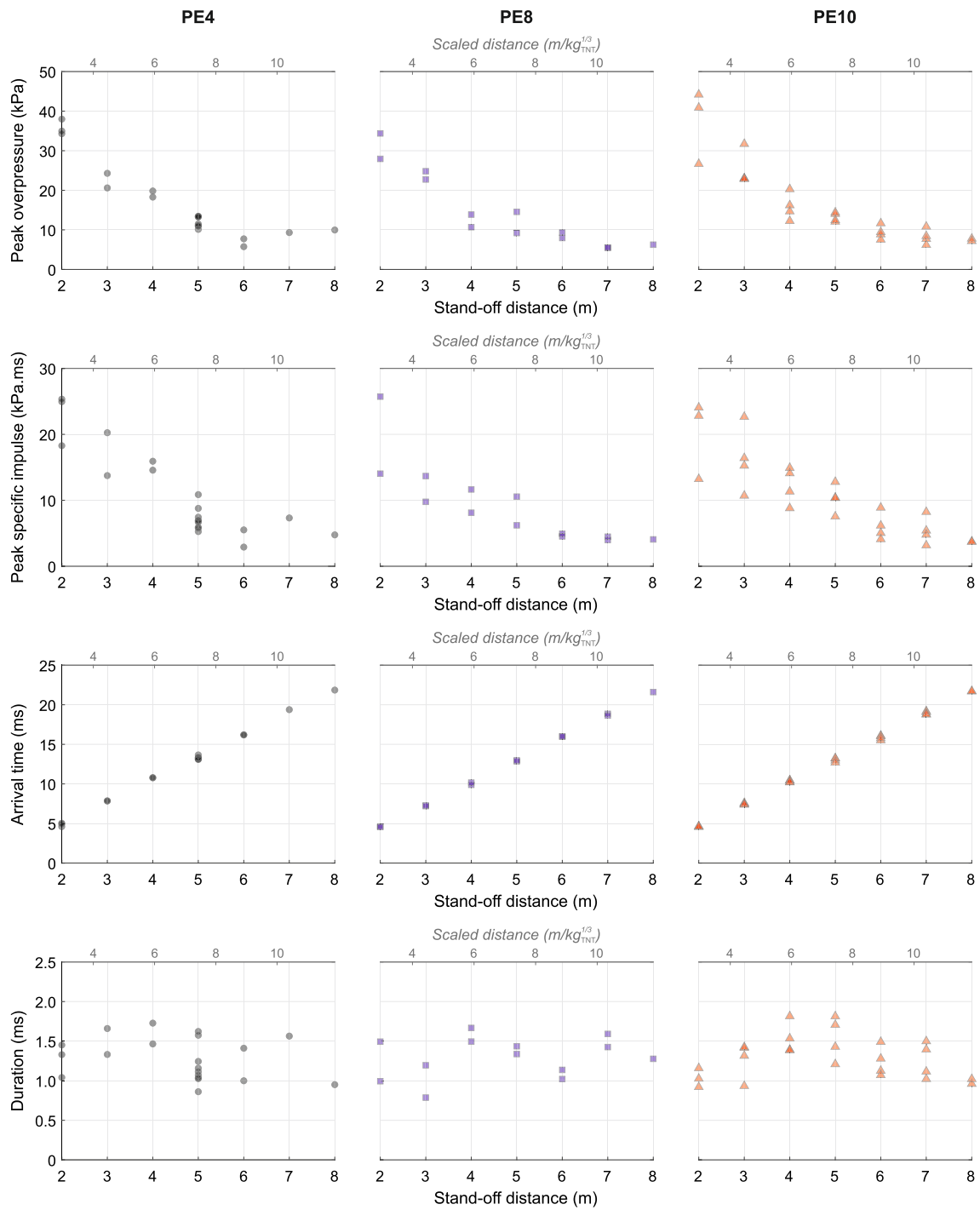
Fig. 4 Compiled secondary shock parameters: peak pressure, p^*; peak specific impulse, i^*; arrival time, t_a^*; and duration t_d^*, from experimental data [45] using 250 g of PE4, PE8, and PE10 at varied stand-off distances. The corresponding scaled distance values have also been included using the TNT_e values listed in Table 1

Table 2 Summary of the experimental datasets used to determine c and dt_{lag} ("train") and subsequently assess the performance of the model ("test")

Stand-off, R (m)	Charge mass, W (kg)	Explosive	No. data points	Source	Data type
2	0.25	PE4	3	[45]	Train
3			2		
4			2		
5			9		
6			2		
7			1		
8			1		
2	0.25	PE8	2		
3			2		
4			2		
5			2		
6			2		
7			2		
8			1		
2	0.25	PE10	3		
3			4		
4			4		
5			4		
6			4		
7			4		
8			2		
2	0.25	PE4	1	[37]	Test
4			1		
6			1		
8			1		
10			1		
4	0.18	PE4	2	[60]	
4	0.25		3		
4	0.35		2		
6	0.25		2		
6	0.29		2		
6	0.35		2		
		Total:	76		

ondary shock pressure. Since, in principle, arrival time could be deemed as any time between the beginning of the rise of the peak (typically less than 10 samples from the beginning), a value of 0.05 ms was taken as the limit of uncertainty. Hence, samples were taken from a uniform distribution between y and $y + 0.05$ ms.

Statistical distributions for Monte Carlo sampling are summarised in Table 3. Each parameter is sampled a certain number of times, which is denoted herein as n, i.e., the count of Monte Carlo. In this study, n was chosen as 200 samples, striking a balance between computational expense and statistical rigour. Smaller values of n were found to return slightly different values of c and dt_{lag} on repeat analyses,

Table 3 Summary of statistical distributions used in Monte Carlo sampling, where y is the experimentally measured value or input for each datapoint

Parameter	Distribution	Unit
W	$y + U[-0.1, 0.1]$	g
R	$y + U[-3, 3]$	mm
p^*	$N(y, 0.7^2)$	kPa
t_a^*	$y + U[0, 0.05]$	ms

whereas larger values would return values to the same three significant figures but with increasing analysis times.

3.2 Algorithm for determining c and dt_{lag}

As a reminder, c and dt_{lag} are the two empirically derived parameters for predicting the secondary shock and are defined in general terms as the dummy charge mass, or "charge mass multiplier" (i.e., a representation of the strength of the secondary shock relative to the primary) and time-shift, or "time delay" (i.e., correcting for any model error in arrival time); see Fig. 3.

The algorithm for determining secondary shock parameters c and dt_{lag} is as follows:

0. Generate n random samples of each experimental measure or input: peak secondary shock pressure, p^*; secondary shock arrival time, t_a^*; charge mass, W; and stand-off distance, R, according to the distributions in Table 3.
1. For each p^* value, determine the value of scaled distance, Z, which would result in that value of peak pressure.[11]
2. With each pair of calculated Z and sampled R values, determine dummy charge mass, cW, through the relation $cW = (R/Z)^3$.
3. Determine c by dividing the result by the sampled charge mass, W.
4. Calculate the model secondary shock arrival time using cW and R as inputs to the UFC predictions[12] (Fig. 2b).
5. Determine dt_{lag} by subtracting the model arrival time (determined in the above step) from the sampled experimental arrival time.
6. Divide dt_{lag} by the sampled $W^{1/3}$ to express at Hopkinson–Cranz [38, 39] scale.
7. Repeat steps 1–6 for all n samples.
8. Repeat steps 1–7 for all experimental datapoints.

3.3 Results

Results from the Monte Carlo analysis are shown in Fig. 5. Here, histograms for c and dt_{lag} (top and bottom rows) show the results from n samples and all 58 training datapoints (11,600 in total). The middle row shows box–whisker plots for c as a function of stand-off distance in order to assess whether there is any dependency of c on distance.

Charge mass multiplier is seen to range between 3–5%, with clear peaks in the histograms around these values for

Table 4 Summary of new empirical secondary parameters, c and dt_{lag}

Explosive	c (%)	dt_{lag} (ms/kg$_{TNT}^{1/3}$)
PE4	4.4	1.16
PE8	3.2	0.40
PE10	4.9	0.88

PE8 and PE10. Conceptually, this suggests that the secondary shock contributes to the overall loading history the same amount as a second explosion from a charge with 4% of the original charge mass.

The PE4 results appear slightly skewed by a smaller secondary peak between 6.0–6.5%. On inspection, this appears to be due to significantly larger values of c at $R = 8$ m. Whilst the cause of this is presently unknown, the fact that the PE8 and PE10 box–whisker plots appear invariant of stand-off distance suggests it is not a physically valid feature, and there are no reasonable explanations as to why it should occur for PE4 but not PE8 or PE10. Referring back to Table 2, there are only single datapoints at 7 and 8 m in the PE4 dataset. Removing these two tests saw a marginal reduction in c, and no change to dt_{lag}, so they have been retained here for full transparency. It is hoped that these empirically derived parameters will eventually be revisited, and continually improved, as additional data become available, so the current approach is deemed adequate as a first pass.

Interestingly, despite PE4 and PE8 being notionally similar (see Table 1), there are clear differences in their secondary shock properties, and the explosives cannot rightfully be considered identical. Differences between PE4/8 and PE10 are to be expected since the former are RDX-based and the latter PETN-based.

Model values for PE4, PE8, and PE10 are summarised in Table 4. Here, median values have been chosen as the model parameters as they are judged to be more representative of the results from the Monte Carlo analysis. The median values universally lie closer to the peak of the histograms for c and dt_{lag} for all explosive types, and are clearly less affected by outliers as compared to the mean values.

4 Performance assessment

4.1 Comparison of new model against test dataset

Parameters shown in Table 4 were used to generate new model predictions for comparison against the test dataset, namely 18 tests using 180–350 g PE4 at 2–10 m (see Table 2).
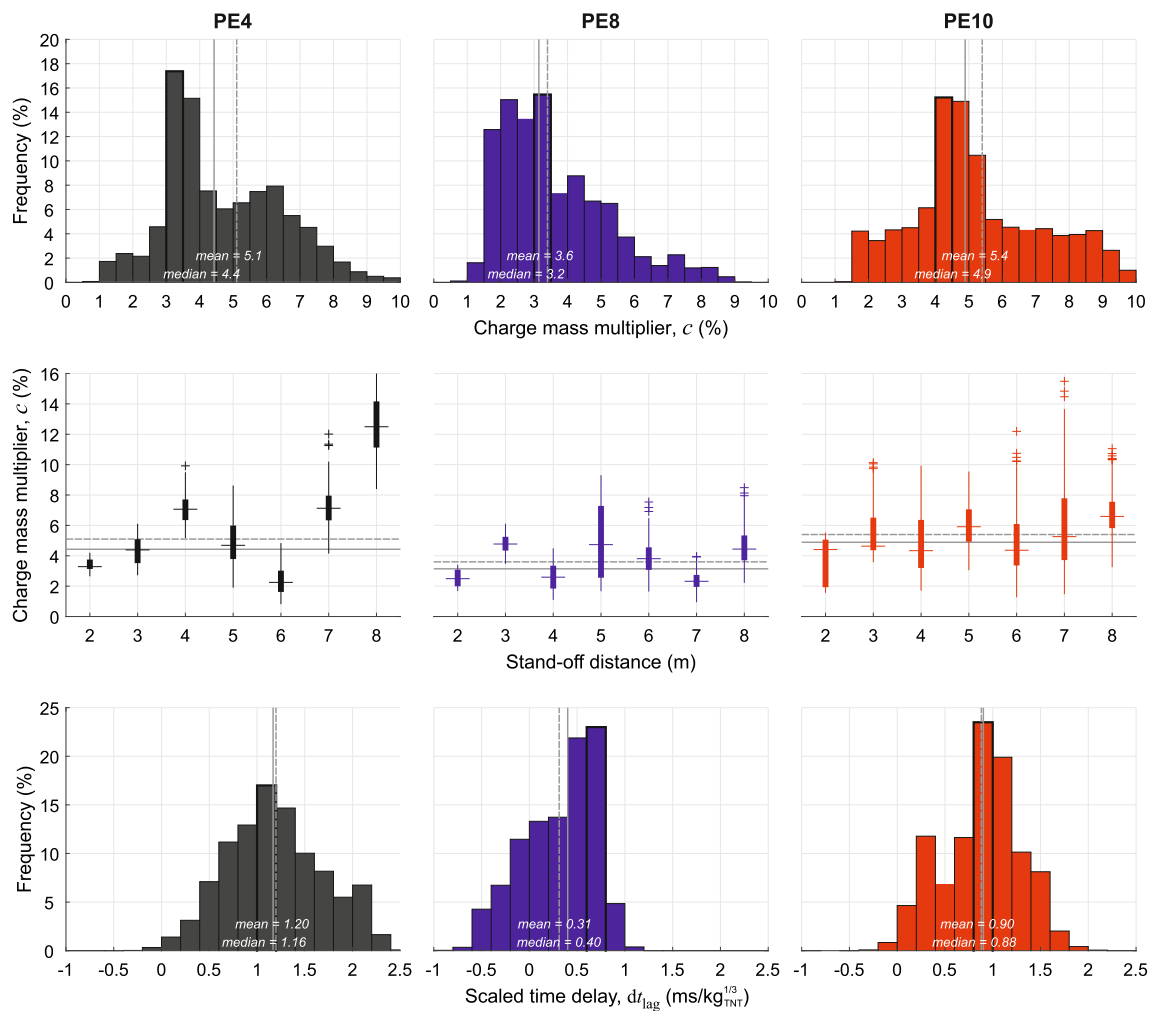
---

[11] In practise, this could be achieved in a number of ways. Since the original Kingery and Bulmash [65] polylogarithmic scaled distance relationships (as well as the simplified [66] and updated versions [67]) are continuous and monotonically decreasing, their inverse function can be found, although these are likely to be quite cumbersome. Alternatively, one could simply interpolate from pre-tabulated pairs of pressure and scaled distance, as was the approach in this study.

[12] Alternatively, simplified [68] or analytical [69] relations may be used.

Fig. 5 Empirical determination of new secondary shock parameters: c and dt_{lag} using Monte Carlo sampling, with the resultant mean and median values overlaid in each plot: (Top row) Histograms of dummy charge mass, or charge mass multiplier, c, for PE4, PE8, and PE10; (Middle row) box–whisker plots for the above, showing how the distributions for c vary with stand-off distance; (Bottom row) histograms of scaled time delay

For each $[R, W]$ pair, p^* and i^*_{net} (9) were determined and compared against the experimental values.[13] Results from these comparisons are shown in Fig. 6. The shaded region around the "new model" values denotes predictions for the range $c \pm 1\%$, i.e., 3.4–5.4% in order to visually assess how sensitive the new model is to choice of dummy charge mass. Also shown are UFC positive phase and negative phase values where appropriate, for context.

The new model follows the experimental trend well, and generally all datapoints are predicted with good accuracy and lie close to, or are within the range predicted by the model. The 2-m test ($Z = 2.99$ m/kg$_{TNT}^{1/3}$) appears to be the largest

outlier for net specific impulse. Since this is an aggregate metric (which combines positive phase, negative phase, and secondary shock), the disagreement cannot be said to be due to inaccuracy of the new model alone. Hence, in the next section two robust performance metrics are introduced to better evaluate the model.

4.2 Performance metrics: MAE and R^2

The performance of the new model is assessed against the dataset using two common metrics: *mean absolute error*, MAE; and *coefficient of determination*, R^2. These two metrics are evaluated for the "standard" UFC model which ignores the secondary shock, and the new model which includes it, and are a measure of the goodness-of-fit of each

---

[13] Here, experimental net impulse is given by the specific impulse value at the end of the negative phase. That is, at $t = t_a + t_d^+ + t_d^-$ as determined by the UFC [32] predicted values. This is a well-defined and easily determined value and consistent for a given $[R, W]$ pair.
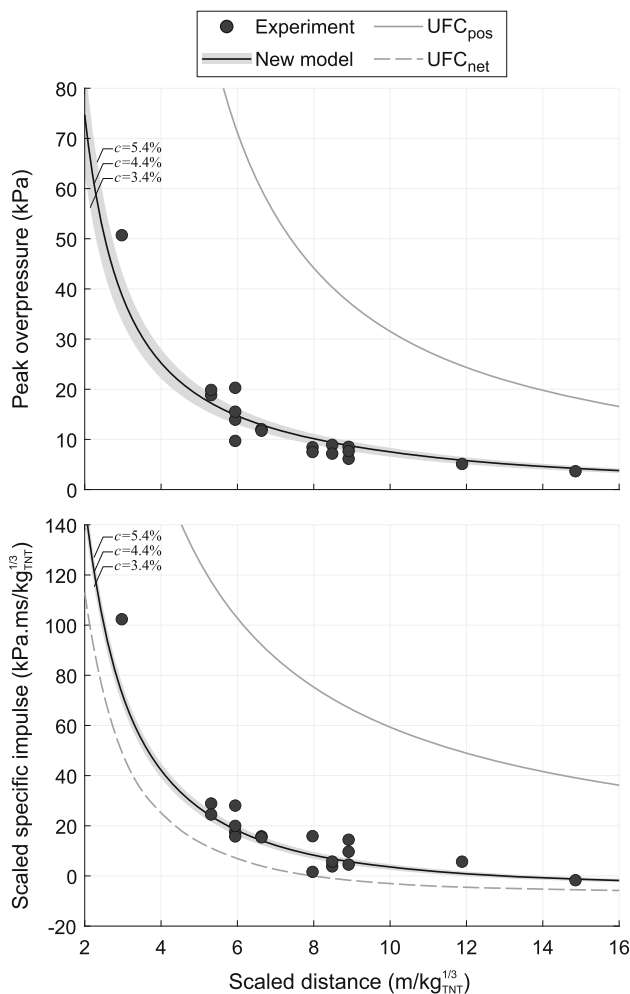
Fig. 6 Experimental and model peak secondary shock overpressure (top) and net specific impulse (bottom) against TNT-equivalent scaled distance for the test dataset. Range of $c \pm 1\%$ shown to illustrate sensitivity to choice of model parameter. UFC primary peak overpressure, positive phase impulse, and net impulse predictions are overlaid for comparison

model with respect to the experimental pressure–time histories.

The positive phase is known to be well predicted by the UFC method [32] and is well represented by the modified Friedlander equation [44], so this performance assessment focusses on the negative phase only. Namely, MAE and R^2 are evaluated for the entirety of the negative phase: $0 \leq \check{t} < t_d^-$, where $\check{t} = t - (t_a + t_d^+)$ as defined previously.

Example traces are shown in Fig. 7 for 180 g at 4 m, 290 g at 6 m, and 250 g at 10 m. All traces are reflected overpressure, and all experiments in the test dataset were with PE4.

It can be seen that the new model reduces the MAE of the negative phase considerably, by between 20–30% in each of the example traces. The coefficient of determination also increases somewhat, which can be easily verified through visual inspection of the traces. There is a considerable por-

tion of the negative phase (roughly one quarter) where the standard UFC model is under-predicting the pressure value by neglecting the secondary shock. Significantly, this results in clear differences between the standard UFC net impulses and the experimental values, with the former being lower by > 10% of the peak value.[14]

The combined effect is that the magnitude of impulse delivered by the total load is under-estimated (i.e., the restorative impulse from the negative phase is *over*-estimated), and dynamic effects of the secondary shock are not accounted for, which may be critical, see Ref. [34] and Sect. 1.2 for further discussion.

Conversely, the new model follows the experimental secondary shock closely, and R^2 values are much closer to unity. There are only small percentage differences in net impulse, approximately 0.5–1% of the peak value in each of the example traces.

Performance metrics for the entire test dataset are summarised in Fig. 8. Here, MAE for the standard UFC predictions and the new model are plotted on the vertical and horizontal axes, respectively. The chart can thus be interpreted as follows: any point *on* the line $y = x$ shows no difference between the UFC approach and the new model, whereas a point to the left of this line shows the new model has reduced MAE to some extent and therefore led to an improvement.

Lines indicating 10, 20, 30, and 40% reductions in MAE are added to aid interpretation, and scaled distance and R^2 of the new model are also shown in this plot for additional context.

Only one of the 18 pressure traces from the test dataset is not improved (MAE increases rather than reduces) when incorporating the secondary shock using the new methodology detailed in this paper. The other 17 pressure traces from the test dataset are more accurately represented using the new methodology, with reductions in MAE approaching 40%, and 10 out of 18 achieving an improvement of > 20%.

R^2 values up to 0.95 are reported, with an average value of 0.87 and a minimum of 0.78; these compare well to the maximum (0.93), mean (0.80), and minimum (0.69) achieved using only the standard UFC model. There appear to be no strong dependencies on scaled distance, suggesting that the method is a robust and accurate means for predicting the contribution of the secondary shock for far-field blast loading ($Z \geq 3$ m/kg$_{TNT}^{1/3}$).

---

[14] It is not appropriate to calculate percentage differences in net impulse due to their proximity to zero, so a more representative measure is percentage of *peak* impulse.
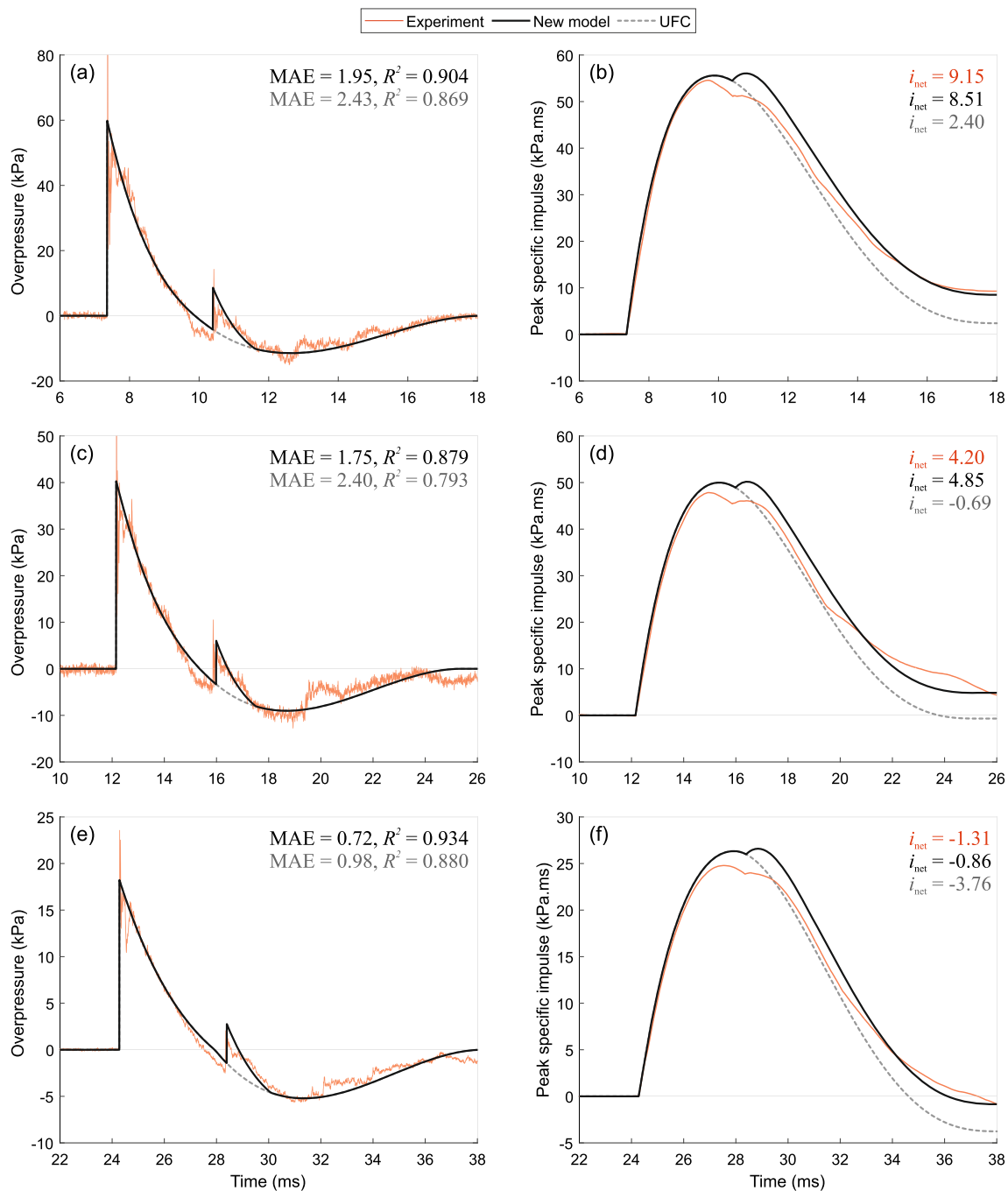
Fig. 7 Example pressure–time (**a**, **c**, **e**) and impulse–time (**b**, **d**, **f**) plots comparing experimental traces with standard UFC predictions and the new model including the secondary shock: **a**, **b** 180 g at 4 m; **c**, **d** 290 g at 6 m; **e**, **f** 250 g at 10 m. Also shown are MAE and R^2 values for each pressure history, as well as net impulse values for comparison

5 Summary and conclusions

The secondary shock has received little attention in the scientific literature, despite it being a common feature in pressure traces from high explosive tests [21]. Whilst established predictive approaches—such as those in UFC 3-340-02—are known to be accurate for the positive [44] and negative [37] phases, there remains no reliable method for predicting the form and magnitude of the secondary shock.

This paper presents a new empirical method for including the effects of the secondary shock, based on superposition of the loading from the original charge mass with addi-
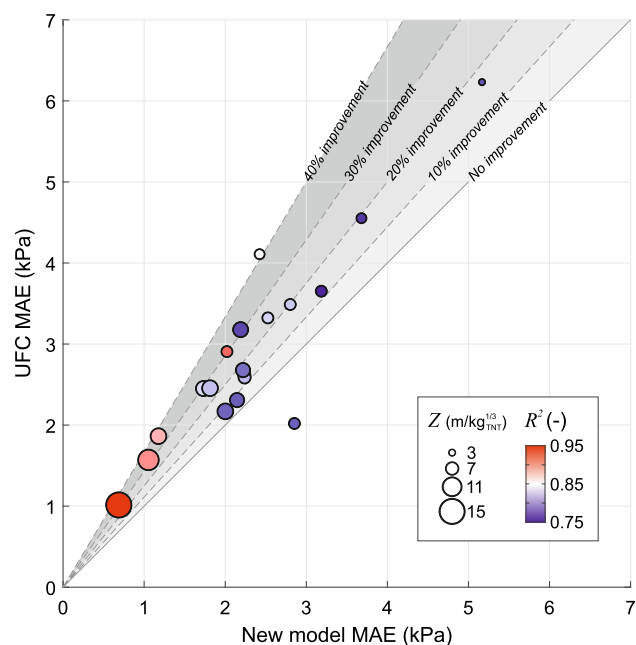
Fig. 8 Negative phase MAE from UFC model (neglecting secondary shock) and new model (incorporating secondary shock). A datapoint on $y = x$ suggests no difference between the two approaches, whereas a point to the left of this line shows an improvement from the new model. Marker sizes indicate TNT-equivalent scaled distance of the pressure trace, and marker colour indicates R^2 of the new model against the experimental trace

tional loading from a secondary explosion originating from a smaller charge mass. The ratio of the masses of the secondary "dummy" charge to the original charge, c, is found empirically using 76 reflected pressure traces using hemispheres of PE4, PE8, and PE10. Additionally, a time-shift parameter, dt_{lag}, is also determined, which corrects the arrival time of the secondary shock on account of the dummy mass being a *surrogate* to the underlying physics.

The 76 datapoints are split into a training group of 58 datapoints, and a test group of 18 datapoints. The first group is used to derive c and dt_{lag} using Monte Carlo sampling to account for experimental uncertainty. Values of c are found to range between 3.2–4.9%, and dt_{lag} between 0.40–1.16 $ms/kg_{TNT}^{1/3}$. Conceptually, this suggests that the secondary shock contributes an additional loading from a charge mass around 4% the size of the original.

The new model is rigorously compared against the test dataset, where it is found that significant reductions in mean absolute error and increases in coefficient of determination of the negative phase are achieved in 17/18 of the cases when compared to those determined from modelling the negative phase only. Improvements of typically 20% and up to 40% are seen, across the full range of far-field scaled distances, giving a high degree of confidence in the new approach.

Whilst the current method has considered reflected pressure traces from hemispheres of ideal plastic explosives only, it can just as easily be applied to any case not included in the above. Future work will look to extend the method to non-ideal and/or non-spherical explosives, and continue to verify the method over a larger range of physical length scales [59].

References

1. Fisher, E., Pittman, J.: Air blast resulting from the detonation of small TNT charges. Technical Report AD208580, NAVORD 2890, Naval Ordnance Lab White Oak MD, USA (1953). https://apps.dtic.mil/sti/tr/pdf/AD0208580.pdf

2. Boyer, D.W.: An experimental study of the explosion generated by a pressurized sphere. J. Fluid Mech. **9**(3), 401–429 (1960). https://doi.org/10.1017/S0022112060001195

3. Dewey, J.M.: The air velocity in blast waves from t.n.t. explosions. Proc. R. Soc. Lond. A **279**(1378), 366–385 (1964). https://doi.org/10.1098/rspa.1964.0110

4. Sadwin, L.D., Swisdak Jr, M.M: Blast characteristics of 20 and 100 ton hemispherical AN/FO charges. Technical Report AD871892, NOLTR 70-32, Naval Ordnance Lab, White Oak, MD, USA (1970). https://apps.dtic.mil/sti/tr/pdf/AD0871892.pdf

5. Ohashi, K., Kleine, H., Takayama, K.: Characteristics of blast waves generated by milligram charges. Proceedings of the 23rd International Symposium on Shock Waves, Fort Worth, USA, 23–27 July (2001). https://www.ifs.tohoku.ac.jp/jpn/shock-coe/papers/issw23/5489p.pdf

6. Mizukaki, T., Wakabayashi, K., Matsumura, T., Nakayama, K.: Background-oriented schlieren with natural background for quantitative visualization of open-air explosions. Shock Waves **24**(1), 69–78 (2014). https://doi.org/10.1007/s00193-013-0465-4

7. Brode, H.L.: Numerical solutions of spherical blast waves. J. Appl. Phys. **26**(6), 766–775 (1955). https://doi.org/10.1063/1.1722085

8. Friedman, M.P.: A simplified analysis of spherical and cylindrical blast waves. J. Fluid Mech. **11**(1), 1–15 (1961). https://doi.org/10.1017/S0022112061000810

9. Sachdev, P.L.: Spherical blast waves produced by sudden expansion of a high pressure gas. In: Shock Waves & Explosions, Chapter 7, pp. 207–236. Chapman and Hall/CRC (2004). https://doi.org/10.1201/9781420035193

10. Liang, S.M., Wang, J.S., Chen, H.: Numerical study of spherical blast-wave propagation and reflection. Shock Waves **12**(1), 59–68 (2002). https://doi.org/10.1007/s00193-002-0142-5

11. US Army Materiel Command, Engineering Design Handbook. Explosions in air part one. Department of the Army, Alexandria, VA, USA, AMCP 706-181 (1974). https://apps.dtic.mil/sti/tr/pdf/ADA003817.pdf

12. Langran-Wheeler, C., Rigby, S.E., Clarke, S.D., Tyas, A., Stephens, C., Walker, R.: Near-field spatial and temporal blast pressure distributions from non-spherical charges: horizontally-aligned cylinders. Int. J. Protect. Struct. 12(4), 492–516 (2021). https://doi.org/10.1177/2041419621101344

13. Edwards, D.H., Thomas, G.O., Milne, A., Hooper, G., Tasker, D.: Blast wave measurements close to explosive charges. Shock Waves 2, 237–243 (1992). https://doi.org/10.1007/BF01414759

14. Rigby, S.E., Tyas, A., Clarke, S.D., Fay, S.D., Reay, J.J., Warren, J.A., Gant, M., Elgy, I.: Observations from preliminary experiments on spatial and temporal pressure measurements from near-field free air explosions. Int. J. Protect. Struct. 6(2), 175–190 (2015). https://doi.org/10.1260/2041-4196.6.2.175

15. Dennis, A.A., Pannell, J.J., Smyl, D.J., Rigby, S.E.: Prediction of blast loading in an internal environment using Artificial Neural Networks. Int. J. Protect. Struct. 12(3), 287–314 (2020). https://doi.org/10.1177/204141962097057

16. Gautier, A., Sochet, I., Lapebie, E., Boubrit, A.: Shock wave propagation in an obstructed area. WIT Trans. Built Environ. 198, 15–27 (2020). https://doi.org/10.2495/SUSI200021

17. Cimpoeru, S.J., Ritzel, D.V., Brett, J.M.: Chapter 1 - Physics of explosive loading of structures. In: Mouritz, A.P., Rajapakse, Y.D.S. (eds.) Explosion Blast Response of Composites, pp. 1–22. Woodhead Publishing, Sawston (2017). https://doi.org/10.1016/B978-0-08-102092-0.00001-7

18. Almustafa, M.K., Nehdi, M.L.: Fundamental review on collision of blast waves. Phys. Fluids 35(3), 031302 (2023). https://doi.org/10.1063/5.0138156

19. Isaac, O.S., Alshammari, O.G., Clarke, S.D., Rigby, S.E.: Experimental investigation of blast mitigation of pre-fractal obstacles. Int. J. Protect. Struct. 15(1), 95–121 (2024). https://doi.org/10.1177/20414196221144066

20. The European Space Agency. Cosmic Microwave Background (CMB) radiation. https://www.esa.int/Science_Exploration/Space_Science/Herschel/Cosmic_Microwave_Background_CMB_radiation. Retrieved 27 Jun 2024

21. Gitterman, Y.: Secondary shock features for large surface explosions: Results from the Sayarim Military Range, Israel and other experiments. Shock Waves 24, 267–282 (2014). https://doi.org/10.1007/s00193-013-0487-y

22. Rigby, S., Gitterman, Y.: Secondary shock delay measurements from explosive trials. Proceedings of the 24th Military Aspects of Blast and Shock (MABS24), Halifax, Nova Scotia, Canada, 19–23 September (2016). https://eprints.whiterose.ac.uk/105006/

23. Budakoğlu, E.: Seismological investigations of fireworks factory explosions in Hendek-Sakarya (Turkey). J. Seismolog. 26(2), 283–299 (2022). https://doi.org/10.1007/s10950-022-10082-z

24. Rae, P.J., McAfee, J.M.: The blast parameters spanning the fireball from large hemispherical detonations of C-4. Propellants Explos. Pyrotech. 43(7), 694–702 (2018). https://doi.org/10.1002/prep.201800071

25. Schwer, L., Rigby, S.: Reflected secondary shocks: Some observations using afterburning. Proceedings of the 11th European LS-DYNA Conference, Salzburg, Austria, 9–11 May (2017). https://eprints.whiterose.ac.uk/116125/

26. Schwer, L, Rigby, S.: Secondary and height of burst shock reflections: Application of afterburning. Proceedings of the 25th Military Aspects of Blast and Shock (MABS25), The Hauge, Netherlands, 23–28 September (2018). https://eprints.whiterose.ac.uk/136091/

27. Anderson, J.G., Perry, S.L., Ritzel, D.V.: Time dependent blast wave properties from shock wave tracking with high speed video. Proceedings of the 24th Military Aspects of Blast and Shock (MABS24), Halifax, Nova Scotia, Canada, 19–23 September (2016). https://mabs.ch/data/documents/24-048.pdf

28. Netherton, M.D., Stewart, M.G.: Risk-based blast-load modelling: techniques, models and benefits. Int. J. Protect. Struct. 7(3), 430–451 (2016). https://doi.org/10.1177/204141961666645

29. Tyas, A., Reay, J.J., Fay, S.D., Clarke, S.D., Rigby, S.E., Warren, J.A., Pope, D.J.: Experimental studies of the effect of rapid afterburn on shock development of near-field explosions. Int. J. Protect. Struct. 7(3), 456–465 (2016). https://doi.org/10.1177/2041419616665931

30. Kirchner, M.R., Kirchner, S.R., Dennis, A.A., Rigby, S.E.: Non-parametric characterization of blast loads. Int. J. Protect. Struct. 15(3), 509–535 (2023). https://doi.org/10.1177/20414196231184581

31. Bogosian, D., Ferritto, J., Shi, Y.: Measuring uncertainty and conservatism in simplified blast models. 30th Explosives Safety Seminar, Atlanta, GA, USA, pp. 1–26 (2002). https://apps.dtic.mil/sti/tr/pdf/ADA526954.pdf

32. US Department of Defence. Structures to resist the effects of accidental explosions. US DoD, Washington DC, USA, UFC 3-340-02 (2008)

33. Ehrhardt, L., Boutillier, J., Magnan, P., Deck, C., De Mezzo, S., Willinger, R., Cheinet, S.: Evaluation of overpressure prediction models for air blast above the triple point. J. Hazard. Mater. 311, 176–185 (2016). https://doi.org/10.1016/j.jhazmat.2016.02.051

34. Hatfield, J.E., Pezzola, G.L., Walker, R.E., Stephens, C.S., Davidson, J.S.: Fragment response of unreinforced concrete masonry walls subjected to blast loading. Int. J. Protect. Struct. 13(2), 161–181 (2022). https://doi.org/10.1177/20414196221080482

35. Halswijk, W.H.C.: BeamBlast: Blast path-finding algorithms. Proceedings of the 16th International Symposium for the Interaction of the Effects of Munitions with Structures (ISIEMS16), Destin, FL, USA, 9-13 November (2015)

36. Bortolan Neto, L.: The Friedlander–Heaviside series for describing pressure-time history of reflected blast waves (2023). Available at SSRN. https://doi.org/10.2139/ssrn.4332008

37. Rigby, S.E., Tyas, A., Bennett, T., Clarke, S.D., Fay, S.D.: The negative phase of the blast load. Int. J. Protect. Struct. 5(1), 1–20 (2014). https://doi.org/10.1260/2041-4196.5.1.1

38. Hopkinson, B.: British Ordnance Board Minutes, 13565 (1915)

39. Cranz, C.: Lehrbuch der Basllistik. Springer, Berlin (1926). https://doi.org/10.2307/3602876

40. Rigby, S.E., Sielicki, P.W.: An investigation of TNT equivalence of hemispherical PE4 charges. Eng. Trans. 62(4), 423–435 (2015). https://doi.org/10.24423/engtrans.266.2014

41. Rickman, Denis D., Murrell, Donald W.: Development of an improved methodology for predicting airblast pressure relief on a directly loaded wall. J. Press. Vessel Technol. 129(1), 195–204 (2006). https://doi.org/10.1115/1.2409317

42. Cheval, K., Loiseau, O., Vala, V.: Laboratory scale tests for the assessment of solid explosive blast effects. Part I: Free-field test campaign. J. Loss Prev. Process Ind. 23(5), 613–621 (2010). https://doi.org/10.1016/j.jlp.2010.05.001

43. Cheval, K., Loiseau, O., Vala, V.: Laboratory scale tests for the assessment of solid explosive blast effects. Part II: Reflected blast series of tests. J. Loss Prev. Process Ind. 25(3), 436–442 (2012). https://doi.org/10.1016/j.jlp.2011.11.008

44. Rigby, S.E., Tyas, A., Fay, S.D., Clarke, S.D., Warren, J.A.: Validation of semi-empirical blast pressure predictions for far field explosions—is there inherent variability in blast wave parameters? Proceedings of the 6th International Conference on Protection of Structures Against Hazards (PSH14), Tianjin, China, 16–17 October (2014). https://eprints.whiterose.ac.uk/81237/

45. Farrimond, D.G., Woolford, S., Tyas, A., Rigby, S.E., Clarke, S.D., Barr, A., Whittaker, M., Pope, D.J.: Far-field positive phase blast parameter characterisation of RDX and PETN based explosives.

Int. J. Protect. Struct. **15**(1), 141–165 (2024). https://doi.org/10.1177/20414196221149752

46. Hargather, M.J., Winter, K.O., Kimberley, J., Wei, T.: A comparison of explosively driven shock wave radius versus time scaling approaches. Shock Waves **33**(6), 449–460 (2023). https://doi.org/10.1007/s00193-023-01149-y

47. Dewey, J.M.: The shape of the blast wave: Studies of the Friedlander equation. Proceedings of the 21st Military Aspects of Blast and Shock (MABS21), Jerusalem, Israel, 3–8 October (2010). https://mabs.ch/data/documents/20-95.pdf

48. Stewart, Mark G., Netherton, Michael D., Baldacchino, Hayden: Observed airblast variability and model error from repeatable explosive field trials. Int. J. Protect. Struct. **11**(2), 235–257 (2020). https://doi.org/10.1177/2041419619871305

49. Farrimond, Dain G., Rigby, Sam E., Clarke, Sam D., Tyas, Andy: Time of arrival as a diagnostic for far-field high explosive blast waves. Int. J. Protect. Struct. **13**(2), 379–402 (2022). https://doi.org/10.1177/20414196211062923

50. Friedlander, F.G.: The diffraction of sound pulses. I. Diffraction by a semi-infinite plane. Proc. R. Soc. A: Math. Phys. Eng. Sci. **186**(1006), 322–344 (1946). https://doi.org/10.1098/rspa.1946.0046

51. Gantes, Charis J., Pnevmatikos, Nikos G.: Elastic-plastic response spectra for exponential blast loading. Int. J. Impact Eng. **30**(3), 323–343 (2004). https://doi.org/10.1016/S0734-743X(03)00077-0

52. Granström, S.A.: Loading characteristics of air blasts from detonating charges. Technical Report 100. Transactions of the Royal Institute of Technology, Stockholm (1956)

53. Karlos, V., Solomos, G., Larcher, M.: Analysis of the blast wave decay coefficient using the Kingery-Bulmash data. Int. J. Protect. Struct. **7**(3), 409–429 (2016). https://doi.org/10.1177/2041419616659572

54. Zadow, C.: Initial development of a simple, fast-running model for replicating blast wave reflection using an image charge. MEng Thesis, Department of Civil and Structural Engineering, University of Sheffield, UK (2020)

55. Mendham, E., Rigby, S.E., Farrimond, D.G., Tyas, A., Pezzola, G.: Far field blast parameters from cuboidal charges. Proceedings of the The 4th International Conference on Structural Safety Under Fire & Blast Loading (CONFAB 2024), London, UK, 9–10 September (2024). https://eprints.whiterose.ac.uk/216964/

56. Xiao, W., Andrae, M., Gebbeken, N.: Air blast TNT equivalence concept for blast-resistant design. Int. J. Mech. Sci. **185**, 105871 (2020). https://doi.org/10.1016/j.ijmecsci.2020.105871

57. Dewey, M.C., Dewey, J.M.: The physical properties of the blast wave produced by a stoichiometric propane/oxygen explosion. Shock Waves **24**(6), 593–601 (2014). https://doi.org/10.1007/s00193-014-0521-8

58. Tyas, A.: Blast loading from high explosive detonation: what we know and what we don't know. Proceedings of the 13th International Conference on Shock and Impact Loads on Structures (SILOS13), Guangzhou, China, 14–15 December (2019)

59. Rigby, S., Mendham, E., Farrimond, D., Tyas, A., Pickering, E.G., Pezzola, G.: Re-visiting the secondary shock. Proceedings of the 19th International Symposium on Interaction of the Effects of Munitions with Structures (ISIEMS 19), Bonn, Germany, 9–13 December (2024). https://eprints.whiterose.ac.uk/219346/

60. Rigby, S.E., Fay, S.D., Tyas, A., Warren, J.A., Clarke, S.D.: Angle of incidence effects on far-field positive and negative phase blast parameters. Int. J. Protect. Struct. **6**(1), 23–42 (2015). https://doi.org/10.1260/2041-4196.6.1.23

61. Farrimond, D.G., Woolford, S., Barr, A.D., Lodge, T., Tyas, A., Waddoups, R., Clarke, S.D., Rigby, S.E., Hobbs, M.J., Willmott, J.R., Whittaker, M., Pope, D.J., Handy, M.: Experimental studies of confined detonations of plasticised high explosives in inert and reactive atmospheres. Proc. R. Soc. A: Math. Phys. Eng. Sci. **480**(2294), 20240061 (2024). https://doi.org/10.1098/rspa.2024.0061

62. Rigby, S.E., Tyas, A., Bennett, T., Fay, S.D., Clarke, S.D., Warren, J.A.: A numerical investigation of blast loading and clearing on small targets. Int. J. Protect. Struct. **5**(3), 253–274 (2014). https://doi.org/10.1260/2041-4196.5.3.253

63. Bogosian, D., Powell, D., Ohrt, A.: Consequences of applying objective methods for selecting peak pressure from experimental data. Proceedings of the 18th International Symposium for the Interaction of the Effects of Munitions with Structures (ISIEMS18), Panama City, FL, USA, 21–25 October (2019)

64. Chiquito, M., Castedo, R., López, L.M., Santos, A.P., Mancilla, J.M., Yenes, J.I.: Blast wave characteristics and TNT equivalent of improvised explosive device at small-scaled distances. Defence Sci. **69**(4), 328–335 (2019). https://doi.org/10.14429/dsj.69.13637

65. Kingery, C.N., Bulmash, G.: Airblast parameters from TNT spherical air burst and hemispherical surface burst. Technical Report ARBRL-TR-02555, U.S Army BRL, Aberdeen Proving Ground, MD, USA. OCLC Number: 26785780 (1984)

66. Swisdak, M.M.: Simplified Kingery airblast calculations. 26th Department of Defense Explosives Safety seminar. Miami, FL, USA (1994). https://apps.dtic.mil/sti/pdfs/ADA526744.pdf

67. Shin, J., Whittaker, A.S., Cormie, D.: Incident and normally reflected overpressure and impulse for detonations of spherical high explosives in free air. J. Struct. Eng. **141**(12), 04015057 (2015). https://doi.org/10.1061/(ASCE)ST.1943-541X.0001305

68. Rigby, S.E., Lodge, T.J., Alotaibi, S., Barr, A.D., Clarke, S.D., Langdon, G.S., Tyas, A.: Preliminary yield estimation of the 2020 Beirut explosion using video footage from social media. Shock Waves **30**(6), 671–675 (2020). https://doi.org/10.1007/s00193-020-00970-z

69. Díaz, J.S., Rigby, S.E.: Blast wave kinematics: theory, experiments, and applications. Shock Waves **32**(5), 405–415 (2022). https://doi.org/10.1007/s00193-022-01089-z